

論文 / 著書情報
Article / Book Information

Title	Fluid drag reduction by penguin-mimetic laser-ablated riblets with yaw angles
Authors	Ryosuke Saito, Takeshi Yamasaki, Hiroto Tanaka
Citation	Bioinspiration & Biomimetics, Vol. 17, Issue 5,
Pub. date	2022, 8
DOI	https://doi.org/10.1088/1748-3190/ac7f71
Copyright	This is the Accepted Manuscript version of an article accepted for publication in Bioinspiration & Biomimetics. IOP Publishing Ltd is not responsible for any errors or omissions in this version of the manuscript or any version derived from it. The Version of Record is available online at https://doi.org/10.1088/1748-3190/ac7f71 .
Creative Commons	See next page.

License



Creative Commons: CC BY-NC-ND

Fluid drag reduction by penguin-mimetic laser-ablated riblets with yaw angles

Ryosuke Saito¹, Takeshi Yamasaki², and Hiroto Tanaka¹

¹Department of Mechanical Engineering, School of Engineering, Tokyo Institute of Technology, 2-12-1 Ookayama, Meguro-ku, Tokyo, 152-8550 Japan

²Yamashina Institute for Ornithology, 115 Konoyama, Abiko-shi, Chiba, 270-1145 Japan

Keywords

penguin, feather, riblet, hydrodynamics, drag reduction, laser ablation

Abstract

The bodies of penguins, which swim underwater to forage, are densely covered with feathers, in which the barbs are oriented in the longitudinal direction. We hypothesize that these barbs act as riblets and reduce friction drag during swimming. Considering various real-world swim conditions, the drag reduction effect is expected to be robust against changes in the flow speed and yaw angle relative to the flow. To test this hypothesis, we created trapezoidal riblets based on the morphology of these barbs and measured the drag of flat plates with these fabricated riblets in a water tunnel. The spacing, width, and height of the barbs were found to be approximately 100, 60, and 30 μm , respectively. This spacing resulted in a nondimensional spacing s^+ of 5.5 for a typical penguin swimming speed of 1.4 m/s. We fabricated four types of riblets on polyimide films by UV laser ablation. The first was a small-scale riblet for which the spacing was decreased to 41 μm to simulate the surface flow condition of the usual and slower swim behaviors in our water tunnel. The other three were manufactured to the actual scale of real barbs (spacing of 100 μm) with three different rib ridge widths: 10, 25, and 50 μm . Yaw angles of 0°, 15°, 30°, and 45° were also tested with the actual-scale riblets. The drag reduction rate of the small-scale riblet was maximized to 1.97% by the smallest s^+ of 1.59. For all three actual-scale riblets, increasing the yaw angle from zero to 15° enhanced the drag reduction rate for the full range of s^+ up to 13.5. The narrow-ridge riblet reduced

drag at an even higher yaw angle of 45°, but the drag increased with zero yaw angle. Overall, the medium-ridge riblet, which was representative of the barbs, was well-balanced.

1. Introduction

Penguins demonstrate excellent swimming abilities, including high-speed swimming during foraging, long travel distances, and deep diving. For example, the swim speed of penguins is approximately 2 m/s, and their speed per body mass is faster than that of other breath-hold divers, such as marine mammals and sea turtles (Watanabe *et al.*, 2011). The Fiordland penguin *Eudyptes pachyrhynchus* can swim an average of 80 km per day and a maximum of 6800 km in 70 days (Mattern *et al.*, 2018). The diving depth of emperor penguins *Aptenodytes forsteri* reaches 564 m (Wienecke *et al.*, 2007). The king penguin *Aptenodytes patagonicus* can dive for up to 27 minutes (Sato *et al.*, 2011). Since penguins spend a long time in the sea, it is natural to expect that their bodies have evolved to reduce fluid drag to save energy.

The body surface of penguins is densely covered by feathers with no gaps (Williams *et al.*, 2015; Kulp *et al.*, 2018). The micro barbs (i.e., hairs) of each feather exposed on the surface are oriented along the longitudinal direction of the body. Here, we hypothesized that the body surface texture created by the feathers can act as a riblet that suppresses or even reduces fluid frictional drag in swimming penguins. Moreover, considering the body undulation due to the flapping of the wings by the penguins (Clark and Bemis, 1979; Harada *et al.*, 2021), it is favorable that the drag reduction function is effective not only when the barbs are parallel to the flow but also when the barbs have a yaw angle to the flow to some extent. Additionally, penguins change their swim speed from slow resting to fast foraging, demanding robustness of the drag reduction to the flow speed.

Previous biological studies claimed that the body feathers have water repellent and heat insulating functions to prevent heat loss to cold water (Kostina *et al.*, 1996; Gill *et al.*, 2007; Dawson *et al.*, 1999). On the other hand, drag reduction effect of the body feathers has never been investigated to date. Regarding the body drag, Lovvorn *et al.*, 2001 compared the drag of frozen body specimens of diving seabirds, including little penguin *Eudyptula minor*, with their smooth replica models by towing experiments in a water tank. Their results showed that the drag of the frozen specimens was 2-6 times greater than that of the models, suggesting that the body feathers may rather increase the body drag.

Previous study of drag reduction effect of hairy body surface of diving animals other than seabirds is sparse too. Itoh *et al.*, 2006 measured the friction drag of a seal fur attached to a wall of a water channel. In

contrast to the above seabird study, they reported that friction drag was reduced up to 12% by the seal fur. However, morphological parameters of the hairs such as spacing and cross-sectional shape were not investigated.

In engineering, drag reduction is important in industrial transportation equipment such as cars, aircraft, trains, and ships for saving a tremendous amount of energy (Hefner, 1988). It has been reported that friction drag accounts for 10% of the total fluid drag for cars, 30–50% for aircraft, 40–90% for trains, and 70% for ships (Bushnell *et al.*, 1990; Ido and Kohama, 2005; Maeda, 2011). Therefore, determining the mechanism of frictional drag and revealing the superior characteristics of animals found in nature may provide a new approach to reducing frictional drag.

As a bioinspired surface structure for reducing friction drag, riblets have been widely studied since the 1980s, as thoroughly reviewed by Dean *et al.*, 2010 and Bixler and Bhushan, 2013. The riblet was originally inspired by the denticles of migratory sharks. Generally, the riblet is composed of an array of micro ribs oriented parallel to the direction of the surface flow. The ribs with appropriate spacing lift streamwise vortices in the turbulent boundary layer away from the surface, and then the velocity gradient decreases, resulting in a reduction in the viscous friction. Although various cross-sectional shapes of the rib have been investigated, such as thin rectangular (blade), triangular (sawtooth), and scalloped ribs, the simple rectangular blade ribs with appropriate spacing was found to achieve the maximum drag reduction of approximately 10% (Bechert *et al.*, 1997). An array of realistic replicated shark denticles was also tested, resulting in a maximum 3% reduction in the friction drag (Bechert *et al.*, 2000 a). Note that this replica was scaled up 100 times to assess drag in an oil channel.

While experimental application of the riblets to some aircraft and ships for more than thirty years has proved the feasibility of this approach, riblets have still not been widely adopted in aircraft and ships. Airbus covered an A320 aircraft with triangular riblet films produced by 3M, demonstrating that the total drag was reduced by 2% (Szodruch, 1991). Recently, Lufthansa Technik and BASF announced that Lufthansa Cargo's entire freighter fleet of Boeing 777F will be covered with riblet films called AeroShark, to obtain expected fuel savings of more than 1% (Lufthansa Technik, 2021). The 3M riblet film was also attached to a race yacht of the winner of America's cup in 1987 (NASA Langley Research Center, 1993).

For practical usage of the riblets, robustness to variation in flow angle is desired. Previous experimental investigations on the yaw angle (the angle between the riblet and the flow directions) of the riblet have demonstrated that the rate of drag reduction decreased with increasing yaw angle (Walsh and Lindemann, 1984; Hage *et al.*, 2001). The drag increased when the yaw angle was 20° or higher (Hirschel *et al.*, 1988; Enyutin *et*

85 *al.*, 1991). A study using numerical simulations of blade riblets in channel flow also reported that the total drag
86 with a yaw angle of 30° was larger than that without riblets, where the friction drag decreased but the pressure
87 drag increased (Zhang and Yin, 2019).

88 A riblet with a herringbone pattern inspired by the flight feathers of birds was recently studied, where each
89 rib had a yaw angle to the flow. Chen *et al.*, 2014 a, reported that a triangular riblet with a herringbone pattern
90 with a yaw angle of 30° was used to realize a remarkable drag reduction of 17%. The reduction rate increased to
91 20% upon the implementation of a spatial distribution of the rib height. By contrast, the numerical simulation of
92 blade riblets with similar herringbone patterns showed a significant increase in the drag (Benschop and Breugem,
93 2017). We note that the 3-D (three-dimensional) shape of the flight feather is different from that of the body
94 feather of penguins. That is, the flight feather consists of a thick circular rachis, blade-like barbs, and plate-like
95 barbules, while in penguin body feathers both the rachis and barbs have semicircular cross-sections and there are
96 no barbules at the exposed region.

97 The fabrication of small riblets with a wide area is challenging. For air or water flow, the typical spacing
98 of the ribs is on the submillimeter scale. Thus, the fabrication method is an important issue in experimental studies
99 and applications. For example, previous studies employed CNC (computer numerical control) milling (Sasamori,
100 *et al.*, 2014; Jung and Bushen, 2010), carving with a rotary blade (Chen *et al.*, 2014 b; Denkena *et al.*, 2010), and
101 embossing with a micropatterned belt template (Stenzel *et al.*, 2011; Kordy 2015). Point processing of the milling
102 procedure can be applied to realize an arbitrary pattern but requires excessive machining time due to the tiny
103 diameter of the mill. For the rotary blade and embossing processes, it is difficult to change the pattern and cross-
104 sectional shape of the rib, requiring the recreation of the blade or template. For fast fabrication, scanning laser
105 ablation was used to create a riblet with a spacing of 300 μm (Kaakkunen *et al.*, 2018; Tiainen *et al.*, 2020).
106 However, the fabrication error in the rib height was considerable.

107 In this paper, we experimentally evaluated the possibility that penguin body feathers function as riblets
108 based on the detailed observations of penguin feathers and the relationship between penguin swimming
109 conditions and feather morphology. We created trapezoidal riblets based on the morphology of the body feathers
110 by employing UV laser scanning ablation and then conducted drag measurements on a flat plate with the riblet
111 in a water tunnel to simulate the surface flow of the swimming penguin. The robustness of this drag reduction
112 function with respect to the yaw angle was also investigated. Moreover, laser-scanning ablation was employed

to fabricate the riblets, enabling the comparison of different cross-sectional rib shapes on an actual scale or even a smaller scale in a small water tunnel.

2. Materials and Methods

2.1. Measurement of penguin body feathers

We measured the spacing of the dorsal barbs in three museum specimens: the king penguin *Aptenodytes patagonicus* (Specimen ID: YIO-01245), Humboldt penguin *Spheniscus humboldti* (Specimen ID: YIO-01278), and little penguin *Eudyptula minor* (Specimen ID: YIO-65171) at the Yamashina Institute of Ornithology, Japan. The longitudinal lengths of the king, Humboldt, and little penguins were 800, 450, and 340 mm, respectively (Figure 1(A)). The barbs of the body feathers were aligned in the longitudinal direction, as shown in Figure 1(B). We measured the barb spacing at six different longitudinal positions for each specimen as follows. First, 1-3 images of the dorsal surface were obtained with a digital microscope (VR-3000, Keyence Corp., Japan) for each longitudinal position. (Example image for the king penguin is shown in Figure 1(C)). The FOV (field of view) was 3.81 by 2.875 mm² and 1024 by 768 pixels in resolution. Then, we calculated the spacing of the barbs, s_{Barb} , at 1-4 different locations in each image by dividing the length of the measured section by the number of barbs at each measurement location. The width of the barbs, w_{Barb} , was also measured at the same locations based on the pixel size.

A cross-section of the barbs on a dorsal feather of the gentoo penguin *Pygoscelis papua* was observed by SEM (scanning electron microscopy). The feathers were collected at Nagasaki Penguin Aquarium (Nagasaki, Japan) during the molting period in August 2018 (Figure 1(D)). The distal black part was exposed on the surface, and there were no barbules in this area. We manually cut the central barbs at approximately 3 mm from the tip with a scalpel to expose the cross-sections, followed by imaging with an SEM (VE-8800, Keyence Corp., Japan). The obtained images demonstrate that the cross-sections of the barbs are flattened where the width of the bottom is larger than the width of the top (Figure 1(E, F)), which is similar to an observation made in a previous report (Kulp *et al.*, 2018). The width and height were approximately 60 μm and 30 μm , respectively.

2.2. Design parameters of the riblet

We model the cross-section of the rib as a trapezoid (Figure 2), where a , b , and h represent the width of the ridge, width of the base, and height, respectively. s is the spacing of the riblet. Based on the observation of the cross-sections of the barbs, the height-to-width ratio of the rib, h/b , was set to 0.5.

In this study, we tested four different cross-sectional shapes of riblets. Three of them were similar in size to the real barbs, while the ridge widths were different from each other. Hereafter, they are named “wide-ridge riblets”, “medium-ridge riblets”, and “narrow-ridge riblets”. The effect of the cross-sectional shape of the rib was evaluated by comparing these three shapes. The other riblet was smaller than the real barbs to simulate the surface flow of swimming penguins in our water tunnel setup. Hereafter, we call this riblet a “small-scale riblet”. On the other hand, the surface flow for wide-ridge, medium-ridge, and narrow-ridge riblets without a reduction in size corresponds to a higher swimming speed. The actual design values are described in subsection 3.2. We note that we were not able to control the cross-sectional shape of the rib at the small scale.

To investigate the effect of the yaw angle on each rib shape, wide-ridge, medium-ridge, and narrow-ridge riblets with the yaw angles of 15° , 30° , and 45° , respectively, were fabricated.

2.3. Fabrication process of the riblet sheets

To realize riblets with different cross-sectional shapes and spacings, we employed UV (ultraviolet) laser-scanning ablation of polyimide films (thickness of $125\text{ }\mu\text{m}$; Kapton, Du Pont-Toray Co., Ltd., Japan). Since the film is flexible, the product can be attached to a curved surface. Our system (OLMUV-355-7 W-K, OPI Corp., Japan) can scan with a DPSS (diode-pumped solid-state) nanosecond laser (Nd: YVO₄; 355 nm; 7 W; AONano Compact 355-7-50-V, Advanced Optwave Corp., USA) using 2-axis galvanometer mirrors (GM-1015, Canon Inc., Japan). The theoretical diameter of the focusing spot was less than $15\text{ }\mu\text{m}$. By ablating the grooves between each rib with an appropriate spacing between each path of the laser, various riblet spacings and cross-sectional rib shapes were realized. Moreover, we defocused the laser by lifting the surface up by 0.5–1.5 mm from the focal plane so that the ablated surface became smooth. The actual parameters of the laser scanning process are described in subsection 3.2. We note that it is possible to create riblets with arbitrary planar patterns, if needed, because the scanning path is not limited to straight lines but can be used to realize arbitrary curves.

A 24.375 mm by 40 mm riblet area was created in our process. By shifting the worktable of the laser system in the horizontal plane, a 120 mm by 97.5 mm riblet sheet was obtained (Figure 3(A)). For drag

measurements with a varying yaw angle, an 80 mm by 65 mm sheet was cut out from the riblet sheet at the angles of 15°, 30°, and 45° (Figure 3(B)).

2.4. Drag measurement of a flat plate in a water tunnel

The fabricated riblet sheets were attached to both sides of a rigid and flat 1-mm-thick stainless steel (SUS304) plate with double-sided tape (General double-coated adhesive tape, Nitoms, Inc., Japan). As a reference smooth flat plate, polyimide sheets without any laser ablation were attached to the same flat stainless steel plate.

The drag of the plate was measured using a water tunnel (PT-100 Kai, West Japan Fluid Engineering Laboratory Co., Ltd., Japan). The length, height and width of the measurement section were 1000, 200, and 300 mm, respectively. The maximum flow speed was 2.0 m/s.

A 240 mm by 195 mm riblet area was formed by arraying 2 by 2 straight riblet sheets (size of the single sheet: 120 mm by 97.5 mm) or 3 by 3 angled riblet sheets (size of the single sheet: 80 mm by 65 mm) (Figure 4(B)). These riblet sheets were carefully attached to both sides of the plate with double-sided tape. The thickness of the double-sided tape on a single side was approximately 100 μm . A tripping wire made of a 1-mm-diameter metal rod was also glued at a position 10 mm from the leading edge to make the boundary layer turbulent. The plate was fixed to a two-axis load cell (LMC-21426–10N, Nissho-Electric-Works Co., Ltd., Japan) via an attachment part and square bar. The load cell was mounted on a rotation stage so that its x -axis was parallel to the flow and y -axis was vertical to the flow. The angle of attack of the plate was adjusted to zero using the rotational stage. The zero angle of attack was determined as the angle where both the perpendicular (y) and parallel (x) forces were minimized while monitoring the output from the load cell with a certain flow speed. The plate was inserted into a closed channel of the water tunnel from the top through a slit that was 250 mm long and 7 mm wide. The gap between the bottom edge of the plate and the bottom of the channel was set to 10 mm; thus, the single-side area, S , of the riblet surface exposed to the flow was 45600 mm^2 (240 mm in length and 190 mm in height). We note that the water level was set to be approximately 10 mm above the top of the slit to suppress the ejection of the water from the slit when the flow speed was 1 m/s or higher.

The output signal of the x -axis of the load cell was acquired to a PC (personal computer) via an AD (analog-to-digital) converter (USB-6343, National Instruments Corp., USA) at a sampling rate of 1000 Hz. The

natural frequency of the system, checked by hammering, was 18.9 Hz. Thus, the raw data were digitally smoothed with a low-pass filter, for which the cutoff frequency was 15 Hz in the postprocessing.

A single measurement of drag is conducted as follows. First, the initial force value at 0 m/s was obtained as a time-average value of the smoothed data over 10 sec, followed by an increase in the flow speed to the target speed. After the stabilization of the flow speed as evaluated by the stabilization of the output signals, the final force value at the target speed was obtained as a time-average value over 10 sec. Finally, the variation from the initial force at 0 m/s to the force at the target speed was obtained as the drag at the target speed. The flow speed was then decreased to 0 m/s and stabilized for the next measurement.

In a series of measurements, the drag at the flow speeds of 0.5, 1.0, 1.5, and 2.0 m/s was measured. We conducted three series of measurements for all of the actual-scale riblet plates and the smooth plate in a day and repeated the same set of measurements on three successive days. We also performed the measurements for the small-scale riblet plate in another three successive days in the same manner. Hence, a total of nine data samples were obtained for each plate at each flow speed.

The drag reduction rate, DR (%), was calculated as

$$DR = \frac{F_{\text{Riblet}} - F_{\text{Smooth}}}{F_{\text{Smooth}}} \times 100 \quad (1)$$

where F_{Smooth} is the drag of the flat plate with the smooth films and F_{Riblet} is the drag of the flat plate with the riblet films.

The uncertainty analysis was conducted following the standard procedure (ANSI/ASME, 1987). We considered the variation of the nine measurements and the nonlinearity of the load cell. The most significant factor was the nonlinearity of the load cell, which was 0.02% of the capacity (2 N) according to the certificate sheet of the load cell. For example, the uncertainty, U_{RSS} (95% coverage), of the drag measurement was approximately 0.0023 N for the smooth flat plate and was approximately 0.0032 N for the small-scale riblet at a 2.0 m/s flow speed. The uncertainty of DR , δ , was calculated using the error propagation law as

$$\delta = |DR| \sqrt{\left(\frac{\sqrt{\delta_{\text{Riblet}}^2 + \delta_{\text{Smooth}}^2}}{F_{\text{Riblet}} - F_{\text{Smooth}}} \right)^2 + \left(\frac{\delta_{\text{Smooth}}}{F_{\text{Smooth}}} \right)^2} \quad (2)$$

where δ_{Riblet} is the measurement uncertainty of a flat plate with a riblet film and δ_{Smooth} is the measurement uncertainty of a flat plate with a smooth film.

2.5. Nondimensional fluid dynamics parameters

Flow around a swimming penguin was scaled to the plate with a riblet by considering the Reynolds number (Re) and mean thickness of the viscous sublayer of the turbulent boundary layer, $\delta_{\ell, \text{mean}}$.

We assumed the flow conditions of a swimming penguin, as shown in Table 1. The body length, swimming speed, and water temperature are similar to those in our previous kinematic measurement of a gentoo penguin in usual swimming behaviors at an aquarium. These flow conditions are almost the same as those measured by Harada *et al.* (Harada *et al.*, 2021). The kinematic viscosity, ν , of sea water was estimated through linear interpolation between the data for 0°C and 20°C, assuming a temperature of 15°C and salinity of 3.5% (Bullard E., 2017). The resultant Reynolds number for the body length was 6.75×10^5 .

To realize the Reynolds number of the penguin using the 240-mm-long plate in the water tunnel, the flow condition of the water tunnel was determined, as shown in Table 1. When the flow speed was 2.0 m/s, the Reynolds number (6.64×10^5) was similar to that of the model penguin in Table 1 (6.75×10^5).

Assuming that the turbulent boundary layer starts at the leading edge, the thickness of the viscous sublayer, δ_{ℓ} , for a flat plate is empirically expressed as

$$\delta_{\ell} \approx 5 \frac{\nu}{u_{\tau}} \quad (3)$$

$$u_{\tau} = \sqrt{\frac{\tau_w}{\rho}} \quad (4)$$

where u_{τ} (m/s) is the friction velocity in the y direction, τ_w (N/m²) is the shear stress at the wall, and ρ is the density (Schlichting, 1979). By simplifying the penguin model to a flat plate, δ_{ℓ} of the swimming penguin and the flat plate in our water tunnel can be illustrated in Figure 5. The mean thickness, $\delta_{\ell, \text{mean}}$, is 91 mm for the penguin and 37 mm for the plate for the flow conditions in Table 1.

Then, the nondimensional spacing of the barbs or riblet, s^+ , was defined by the $\delta_{\ell, \text{mean}}$ as

$$s^+ = s \frac{5}{\delta_{\ell, \text{mean}}} \quad (5)$$

The swimming speeds of the penguins that we reproduced by equating the value of $\delta_{\ell, \text{mean}}$ in our experiment with flow velocities of 0.5, 1.0, 1.5, and 2.0 m/s in the water tunnel were 0.35, 0.7, 1.05, and 1.41 m/s (small-scale riblet) and 0.95, 1.89, 2.84, and 3.79 m/s (actual-scale riblet). Then, the s^+ values were 1.59, 2.96, 4.27, and 5.53 (small-scale riblet) and 3.87, 7.23, 10.4, and 13.5 (actual-scale riblet), respectively.

3. Results and Discussions

3.1. Morphology of the body feathers and range of s^+

Figure 6 shows the measured spacing of the barbs for the three species of penguins. For the locations 0.1 m or more away from the head, the pooled mean values for each species were 97 μm for the king penguin, 85 μm for the Humboldt penguin, and 75 μm for the little penguin. The differences in the spacings among the species at each location were not significant. Thus, we determined a representative value of the barb spacing of 100 μm .

The measured widths of the barbs are shown in Figure 7. For the locations 0.1 m or more away from the head, the pooled mean values for each species were 42 μm for the king penguin, 31 μm for the Humboldt penguin, and 39 μm for the little penguin. These values are smaller than the bottom width of 60 μm in the SEM image (Figure 1 (F)), possibly because only the top surfaces of the barbs were illuminated and visible under the optical microscope. Therefore, we determined the representative cross-sectional width and height of the barbs to be 60 μm and 30 μm , respectively.

Based on the measured body length of our museum specimens and foraging speed measured in the wild for the king (2.1 m/s), Humboldt (1.9 m/s), and little (1.9 m/s) penguins (Sato *et al.*, 2007; Luna-Jorquera *et al.*, 1999; Watanuki *et al.*, 2006)), the 100 μm spacing of the barbs corresponds to the s^+ values of 7.8, 7.5, and 7.7, respectively. The swimming condition of the gentoo penguin at aquarium shown in Table 1 results in a s^+ of 5.5. These s^+ values are relatively small compared with the s^+ of the previous triangular riblets for maximum drag reduction (approximately 17 (Bechert 1997 *et al.*, 1997)).

3.2. Design and fabrication of the riblets

The design values of the wide-ridge, medium-ridge, narrow-ridge, and small-scale riblets are summarized in the upper half of Table 2. To realize these dimensions, we adjusted the laser path, number of scans, scan speed, power, and defocusing distance (Figure S1 and Table S1).

The 3-D shape of the fabricated riblet was measured with an industrial laser-scanning confocal microscope (SFT-4500, Shimadzu Corp., Japan) at 9 locations in each scanned area, as shown in Figure 3(A). The obtained 3-D images for the central locations are shown in Figure 8, and the measured dimensions are summarized in the lower half of Table 2. The spacing s of the fabricated riblets was almost the same as the design values, due to the high precision of the galvanometer mirrors. The rib ridge width, a , was also realized well with small error. However, the rib height, h , and bottom width, b , were noticeably larger than the target values due to the difficulty in controlling the ablation depth at this microscale with our laser system. The resultant a/b was also smaller than the design. Nevertheless, the relative shape differences among the wide-, medium-, and narrow-ridge trapezoidal riblets were realized.

The resultant h/s for the small-scale, wide-, medium-, and narrow-ridge riblets were 0.5, 0.4, 0.38, and 0.36, respectively; all of these values were larger than the target value of 0.3. A previous study of blade riblets reported that increasing h/s from 0.3 to 0.5 enhances the maximum reduction in drag but reduces the upper limit of s^+ , reducing the drag (Bechert *et al.*, 1997).

We note that shape variation among the nine measured locations in the narrow-ridge riblet was noticeable. At the central location, the ridge width tended to be wider, and there were small ridges on the bottom of the valley (Figure 8(E)), unlike the other eight locations (Figure 8(C)). This variation may be due to the difference in the travel length of the laser from the galvanometer mirrors to the film surface: the travel length for the central location is slightly shorter than those for the other surrounding locations. The wider ridge width than the design value may blur the difference from the medium-ridge riblet in the following experimental results. The small ridges on the valley floor, of which height was approximately 10 μm , may increase the friction drag due to the increase in the surface area.

3.3. Drag of the smooth flat plate

The measured drags of the flat plate with the smooth films, F_{Smooth} , for the flow speeds of 0.5, 1.0, 1.5, and 2.0 m/s are shown in Figure 9. Each error bar represents the uncertainty. The theoretical curve of friction

drag, F_{Friction} , for a flat plate, assuming a turbulent boundary layer, is also illustrated in Figure 9, and is calculated according to

$$F_{\text{Friction}} = 2wl \frac{\rho}{2} u^2 C_f = wlp u^2 \left(0.074 \left(\frac{ul}{\nu} \right)^{-\frac{1}{5}} - \frac{x_T}{l} \left(0.074 \left(\frac{ux_T}{\nu} \right)^{-\frac{1}{5}} - 1.328 \left(\frac{ux_T}{\nu} \right)^{-\frac{1}{2}} \right) \right) \quad (6)$$

where ρ (kg/m³) is the fluid density, u (m/s) is the flow speed, ν (m²/s) is the kinematic viscosity, l (m) is the length of the flat plate, w (m) is the wetted width of the flat plate, and x_T is the distance from the leading edge to the tripping wire where the transition from the laminar boundary layer to the turbulent boundary layer is assumed to occur (Schlichting, 1979). $2wl$ represents the wetted surface area of both sides of the plate. Additionally, C_f is the friction drag coefficient that can be obtained from a one-seventh power law (Schlichting, 1979). The ratios of F_{Friction} to F_{Smooth} ($F_{\text{Friction}}/F_{\text{Smooth}}$) were 0.66, 0.61, 0.58, and 0.56 for 0.5, 1.0, 1.5, and 2.0 m/s, respectively. The difference between F_{Smooth} and F_{Friction} is assumed to be due to the pressure drag derived from the plate thickness of 1 mm. Therefore, if the riblet reduced friction drag while the pressure drag was constant, the reduction rate of the friction drag would be larger than the reduction rate of the drag that includes both the friction and pressure drags.

3.4. Drag change ratio of the small-scale riblet

Figure 10 shows the drag change ratio of the small-scale riblet. The error bars represent the uncertainty U_{RSS} (ANSI/ASME, 1987) (95% coverage). The $\delta_{\ell, \text{mean}}$ -based and Re-based corresponding swimming speeds of the model penguin, where $\delta_{\ell, \text{mean}}$ or Re is identical, are given for each plot. The applied flow speeds of 0.5, 1.0, 1.5, and 2.0 m/s correspond to the swimming speeds of 0.35, 0.70, 1.05, and 1.41 m/s for the model penguin based on the $\delta_{\ell, \text{mean}}$, respectively. The corresponding swimming speeds based on Re (1.66×10^5 , 3.32×10^5 , 4.98×10^5 , and 6.64×10^5) are 0.34, 0.69, 1.03, and 1.38 m/s, which are slightly smaller than those based on δ_{ℓ} where the Re values are 1.66×10^5 , 3.32×10^5 , 4.98×10^5 , and 6.64×10^5 , respectively.

It was found that the drag was reduced by the riblet for all cases. The maximum reduction in the drag was 1.97% at a s^+ of 1.59, corresponding to a swimming speed of approximately 0.35 m/s. The drag reduction at a s^+

of 5.5 representing a 1.4 m/s swimming speed was 0.98%. These results suggest that the penguin feathers reduce drag at the usual or lower swimming speed.

Assuming that the riblets reduce only friction drag and the friction drag can be expressed by equation (6), the maximum reduction rate in friction drag can be calculated as 2.96% at an s^+ of 1.59 and as 1.74% at an s^+ of 5.5 (Figure S2).

In comparison to the previous triangular riblet, the s^+ of the penguin is small. It was reported that the triangular riblet achieves the maximum reduction in drag at an s^+ of approximately 17 when h/s was 0.5 and the ridge angle of the rib was 90° (Bechert *et al.*, 1997). The performance for a small s^+ below 10 was not reported, possibly because a further reduction does not appear to be expected. This small spacing of the penguin barbs may have other functions in addition to drag reduction, such as prevention of heat loss with dense and narrow barbs; this would subsequently prevent gaps between the barbs and minimize their surface area. In fact, penguin feathers exert a heat insulation effect, and it is reasonable to assume that the spacing of the barbs is related to heat transfer as well as drag reduction (Dawson *et al.*, 1999).

3.5. Effect of the rib shape and yaw angle on the drag change ratio

Figure 11 shows the drag change ratio of the wide-, medium-, and narrow-ridge riblets with varying yaw angles. The corresponding swimming speeds of the model penguin based on $\delta_{\ell, \text{mean}}$ and Re are given for each s^+ value. Each error bar represents the uncertainty, U_{RSS} (ANSI/ASME, 1987) (95% coverage).

The medium-ridge riblet, which represents the real barb, reduces drag for yaw angles up to 15° , even at high speeds beyond realistic penguin speeds (Figure 11(A)). Interestingly, the small yaw angle of 15° promoted a further reduction. The maximum reduction of 1.26% was recorded at an s^+ of 3.87 with a yaw angle of 15° . With a yaw angle of 30° , drag was increased for all s^+ . With a yaw angle of 45° , the rate of increase in the drag increased, even though a reduction in drag was observed at an s^+ of 3.87. These results imply that the penguin feathers reduce drag in foraging or higher-speed swimming, allowing a small deviation in the yaw angle up to 15° .

The results for the wide-ridge riblet were similar to those of the medium-ridge riblet until the yaw angle reached 30° (Figure 11(B)). However, a yaw angle of 45° further increased the drag.

Narrow-ridge riblets slightly increased the drag at a yaw angle of zero (Figure 11(C)). A small yaw angle of 15°, however, resulted in a reduction in the drag. In this study, the maximum drag reduction of 1.19% was recorded at an s^+ of 10.4. The drag reduction effect was maintained even with the largest yaw angle of 45° up to an s^+ of 10.4. The maximum drag increase at the largest yaw angle and s^+ was only 0.63%.

The comparison of the three rib shapes for each yaw angle is summarized in Figure 12. When the yaw angle was small, up to 15°, the medium-ridge riblet effectively reduced the drag for a wide range of s^+ values among the three types of riblets, where the corresponding swimming speed of the gentoo penguin was 0.95~3.79. When the yaw angle was not zero and varied strongly up to 45°, the narrow-ridge riblet worked well to reduce the drag. The wide-ridge riblet was the poorest design in that the drag reduction with a small yaw angle was lower and the drag increase with a large yaw angle was drastic.

Assuming that the riblets reduce only friction drag and that the friction drag can be expressed by equation (6), the reduction rate in the friction drag was also calculated, as summarized in Figures S3-S4. The maximum reduction rate in the friction drag was estimated to be 2.08% for the narrow-ridge riblet at an s^+ of 13.5 with a 15° yaw angle.

Comparing these results with the results obtained in previous studies, the maximum drag reduction rate of our riblet of 2.08% marked by the narrow-ridge riblet at an s^+ of 13.5 with a 15° yaw angle is similar to that of the triangular riblets with a ridge angle of 90° ($h/s = 0.5$), which is approximately 3% at an s^+ of approximately 20 (Bechert *et al.*, 1997). However, the narrow-ridge riblet with a yaw angle of 0° increased drag for all s^+ ranges, while the triangular riblets with a ridge angle of 90° used by Bechert *et al.*, 1997 reduced drag up to an s^+ of 32. This difference may be attributed to the smaller value of h/s for our narrow-ridge riblet ($h/s = 0.36$). On the other hand, our medium-ridge riblet reduced drag with a yaw angle of 0° for all s^+ ranges even with a small $h/s = 0.38$, which is also contrary to the result by Bechert *et al.*, 1997 showing that a smaller ridge angle (60°) of the triangular riblet achieved a higher maximum drag reduction rate (approximately 5%) than a larger ridge angle (90°). Hence, a moderate width of the rib ridge may be suitable for a riblet with a small h/s below 0.4.

Regarding the robustness with respect to the yaw angle, a previous experiment by Enyutin *et al.*, 1991 using a triangular riblet ($h/s = 1.0$; ridge angle = 53°) showed that the robustness was improved by reducing s^+ . This trend was also observed in the present study (Figure 12(D)). On the other hand, Enyutin *et al.*, 1991 also reported that the triangular riblet always increased drag when the yaw angle was 40° or greater even with the smallest s^+ , while our narrow-ridge riblet reduced drag at a high yaw angle of 45° when s^+ was small (3.87 and

7.23). This higher robustness of the narrow-ridge riblet may be attributed to the small h/s of 0.36. Moreover, the drag reduction rate of our riblets at a yaw angle of 15° was always greater than that at a yaw angle of 0° regardless of the ridge type (Figure 11), which is in disagreement with a previous study of triangular and scallop riblets that showed that the drag reduction rate always decreased with increasing yaw angle (Hage *et al.*, 2001). This is the unique feature of our penguin-mimetic riblet of the trapezoidal cross-section with small h/s less than 0.4.

In summary, the penguin feather, represented by the small scale and the medium-ridge riblet in this study, reduced drag for the wide range of swimming speeds ranging from 0.35 to 3.79 m/s, allowing small fluctuations up to 15° in the flow angle. By narrowing the ridge width, the robustness with respect to the yaw angle was improved even though the drag increased for the zero yaw angle case.

3.6. Possible effect of other features in real feathers on drag

This paper focuses on the effect of feather barb spacing and cross-sectional shape on drag as a rigid riblet. However, real feathers possess more complex features that may affect drag.

The body feathers partially overlap with another feather behind; thus, a gap in height may exist between the feathers. Bechert *et al.*, 2000 b, reported that an array of thin strings parallel to the flow above the flat surface reduced friction drag in a similar way to the riblets, although the reduction rate was modest up to 1.5%. We note that the diameter of the strings was only 0.08 times the string spacing, while our barb width (60 μm) was comparable to the barb spacing (100 μm). Moreover, overlapping barbs can be regarded as a permeable substrate. Gómez-de-Segura *et al.*, 2019 argued that permeable substrates can reduce turbulent friction drag.

Feathers and barbs may move in response to the surface flow. Sundin *et al.*, 2019 numerically investigated the flexible vertical hairs on the surface in a turbulent boundary layer and reported that stiff and low-mass (i.e., similar density to fluid) hairs with higher resonant frequency than turbulent fluctuation resulted in an increase in drag. Bechert *et al.*, 2000 b, conducted experiments with shark scale models in which each basement was elastically movable with springs and reported that elasticity increased the drag even though the rigid case with the same scales led to a modest reduction in drag up to 3%. By contrast, experimental studies using real shark skin specimens reported that each scale passively flaps up in response to reverse flow, stopping the reverse flow and suppressing further flow separation and pressure drag (Lang *et al.*, 2014; Afroz *et al.*, 2017; Du clos *et al.*, 2018).

Moreover, Davenport *et al.*, 2011 argued that the body drag of penguins is reduced by the release of air bubbles from the feathers because the bubble coating reduces friction drag. They observed that the emperor penguins *Aptenodytes forsteri* always released bubbles from the body during rapid ascent to jump out of the water. We note that the penguins do not release bubbles during descent or during horizontal diving. A video camera attached to the back of a gentoo penguin *Pygoscelis papua* swimming near the water surface captured other swimming Magellanic penguins *Spheniscus magellanicus* in the wild (Handley *et al.*, 2018: Movie S4), showing that the Magellanic penguins did not release bubbles. In our previous investigations of gentoo penguins *Pygoscelis papua* at an aquarium (Harada *et al.*, 2021), no penguin released bubbles in horizontal diving.

The hydrophobicity of the feathers affects friction drag. Min and Kim, 2004, numerically revealed that streamwise slip due to hydrophobicity decreases friction drag. Jung and Bhushan, 2010, experimentally showed that friction drag is decreased by the hydrophobic surface for both laminar and turbulent boundary layers.

In summary, moving feathers presumably increase friction drag, while pressure drag due to flow separation can be suppressed by passive flap-up motion of the feathers. The hydrophobicity of the feathers will reduce friction drag.

4. Conclusion

The function of drag reduction in penguin body feathers modeled as rigid riblets was experimentally evaluated for the first time. Morphological and hydrodynamic modeling demonstrated that the nondimensional riblet spacing s^+ of the feathers was 5.5 for usual swim at aquarium and 8 for foraging swim in wild, which are small compared with conventional riblets. The cross-sectional shape of the rib was modeled to be trapezoidal. The penguin-mimetic riblets were fabricated by UV-laser-scanning ablation of polyimide films with variations in the ridge width and yaw angle. The drag of the flat plate with the film with and without riblets was measured in a water tunnel. The penguin-representative small-scale riblet reduced drag with a decrease in s^+ : the maximum drag reduction rate was 1.97% at an s^+ of 1.59. The actual-scale medium-ridge riblet that was also representative of the feather morphology reduced drag for a wide range of s^+ values from 3.87 to 13.49, corresponding to a wide range of penguin swimming speeds from 0.95 to 3.79 m/s when the yaw angle was equal to or less than 15° . The maximum drag reduction rate of the medium-ridge riblet was 1.26% at an s^+ of 3.87 with a yaw angle of 15° . The narrow-ridge riblet reduced the drag even with a higher yaw angle of 45° when s^+ was 10.4 or less, but the drag increased when the yaw angle was zero. The drag reducing performance of the wide-ridge riblet was inferior to

that of the medium-ridge riblet, particularly when the yaw angle was as large as 45° . Unlike the previously studied triangular riblets, all three wide-, medium- and narrow-ridge riblets showed a higher drag reduction rate at a yaw angle of 15° than at 0° . These results suggest that the body feathers of penguins can reduce drag for the full range of their swim speed, and small fluctuations in the flow angle up to 15° can be advantageous. These penguin-mimetic riblets can be applied to underwater drones operating with various speeds and carrying out different maneuvers.

We note that real feathers include more complex features, such as overlapping, flexibility, movability, and hydrophobicity. Appropriate implementation of such features can enhance the drag reduction performance of the penguin-mimetic riblets.

Acknowledgment

We thank Nagasaki Penguin Aquarium (Nagasaki, Japan) for the gentoo penguin feather sample. We thank the Collaboration Center for Design and Manufacturing for using an industrial laser-scanning confocal microscope. We also thank Hiroaki Kishine for the microscopy and SEM imaging of the feathers. This work was supported by JSPS KAKENHI JP18H05468 and JP20K04283.

References

Afroz, F., Lang, A., Habegger, M., Motta, P. and Hueter, R. (2017). Experimental study of laminar and turbulent boundary layer separation control of shark skin. *Bioinspiration & Biomimetics*, Vol.12, 016009.

ANSI/ASME. (1987). Measurement uncertainty, supplement on instruments and apparatus.

Bechert, D. W., Bruse, M. and Hage, W. (2000 a). Experiments with three-dimensional riblets as an idealized model of shark skin. *Experiments in Fluids*, Vol. 28, pp. 403–412.

Bechert, D.W., Bruse, M. and Meyer, R. (2000 b). Fluid mechanics of biological surfaces and their technological application. *Naturwissenschaften*, Vol. 87, pp. 157-171.

Bechert, D. W., Bruse, M., Hage, W., Vanderhoeven, J. G. T. and Hoppe, G. (1997). Experiments on drag-reducing surfaces and their optimization with an adjustable geometry. *Journal of Fluid Mechanics*, Vol. 338, pp. 59-87.

Benschop, H. O. G. and Breugem, W. P. (2017). Drag reduction by herringbone riblet texture in direct numerical simulations of turbulent channel flow. *Journal of Turbulence*, Vol. 18, No. 8, pp. 717-759.

Bhushan, B. (2019). Lessons from nature for green science and technology: an overview and bioinspired superliquiphobic/philic surfaces. *Philosophical Transactions of the Royal Society A*, Vol. 377, 20180274.

Bixler, G. D. and Bhushan, B. (2013). Fluid drag reduction with shark-skin riblet inspired microstructured surfaces. *Advanced Functional Materials*, Vol. 23, pp. 4507-4528.

Bullard, E. (2017). 2. 7. 9 Physical properties of sea water. Kaye & Laby Table of Physical & Chemical Constants. [Physical properties of sea water 2.7.9 \(archive.org\)](https://www.nist.gov/pml/data/cstr/cstr.cfm?cstr=2.7.9), (Retrieved on February 25, 2021).

Bushnell, D. M. and Hefner, J. N. (1990). Viscous Drag Reduction in Boundary Layers. *Progress in Astronautics and Aeronautics*, Vol.123, pp.203-261.

Chen, H., Rao, F., Shang, X., Zhang, D. and Hagiwara, I. (2014 a). Flow over bioinspired 3D herringbone wall riblets. *Experiments in Fluids*, Vol. 55, No. 1698.

Chen, H., Zhang, X., Ma, L., Che, D., Zhang, D. and Sudarshan, T. S. (2014 b). Investigation on large-area fabrication of vivid shark skin with superior surface functions. *Applied Surface Science*, Vol. 316, pp. 124-131.

Clark, B. D. and Bemis, W. (1979). Kinematics of Swimming of Penguins at the Detroit Zoo. *Journal of Zoology*, Vol. 188, pp. 411-428.

Davenport, J., Hughes, R. N., Shorten, M. and Larsen, P.S. (2011). Drag reduction by air release promotes fast ascent in jumping emperor penguins – a novel hypothesis. *Marine Ecology Progress Series*, Vol. 430, pp. 171-182.

Dawson, C., Vincent, J. F. V., Jeronimidis, G., Rice, G. and Forshow, P. (1999). Heat transfer through penguin feathers. *Journal of Theoretical Biology*, Vol. 199, pp. 291-295.

Dean, B. and Bhushan, B. (2010). Shark-skin surfaces for fluid-drag reduction in turbulent flow: a review. *Philosophical Transactions of the Royal Society A: Mathematical, Physical and Engineering Sciences*, Vol. 368, pp. 4775-4806.

Denkena, B., Köhler, J. and Wang, B. (2010). Manufacturing of functional riblet structures by profile grinding. *CIRP Journal of Manufacturing Science and Technology*, Vol. 3, pp. 14-26.

- Du Clos, K. T., Lang, A., Devey, S., Motta, P. J., Habegger, M. L. and Gemmell, B.J.** (2018). Passive bristling of mako shark scales in reversing flows. *Journal of the Royal Society Interface*, Vol. 15, 20180473.
- Enyutin, G. V., Lashkov, Yu. A., Samoilova, N. V., Fadeev, I. V. and Shumilkina, E. A.** (1991). Influence of downwash on the aerodynamic efficiency of fine-ribbed surfaces. *Fluid Dynamics*, Vol. 26, pp. 31-35.
- Gill, F. B.** (2007). Ornithology 3rd ed., W. H. Freeman and Company.
- Gómez-de-Segura, G. and García-Mayoral, R.** (2019). Turbulent drag reduction by anisotropic permeable substrates - analysis and direct numerical simulations. *Journal of Fluid Mechanics*, Vol. 875, pp. 124-172.
- Hage, W., Bechert, D. W. and Bruse, M.** (2001). Yaw angle effects on optimized riblets. *Aerodynamic Drag Reduction Technologies*, pp. 278-285.
- Handley, J. M., Thiebault, A., Stanworth, A., Schutt, D. and Pistorius, P.** (2018). Behaviourally mediated predation avoidance in penguin prey: *in situ* evidence from animal-borne camera loggers. *Royal Society open science*, Vol. 5, 171449.
- Harada, N., Oura, T., Maeda, M., Shen, Y., Kikuchi, D. M. and Tanaka, H.** (2021). Kinematics and hydrodynamics analyses of swimming penguins: wing bending improves propulsion performance. *Journal of Experimental Biology*, Vol. 224, No. 21.
- Hefner J. N.** (1988). Dragging down fuel costs. *Aerospace America*, January, pp. 14.
- Hirschel E. H., Thiede P. and Monnoyer F.** (1988). Turbulence management applications aspects. *AGARD, Fluid Dynamics of Three-Dimensional Turbulent Shear Flows and Transition*, CP-438.
- Ido, A. and Kohama, Y.** (2005). A study on reducing aerodynamic drag of trains by smoothing the under-floor surface. *Transactions of the Japan Society of Mechanical Engineers. B*, Vol. 71, No. 703.
- Itoh, M., Tamao, S., Iguchi, R., Yokota, K., Akino, N., Hino, R. and Kubo, S.** (2006). Turbulent drag reduction by the seal fur surface. *Physics of Fluids*, Vol. 18, 065102.
- Jung, Y. C. and Bhushan, B.** (2010). Biomimetic structures for fluid drag reduction in laminar and turbulent flows. *Journal of Physics: Condensed Matter*, Vol. 22, 035104.

- Kaakkunen, J. J. J., Tiainen, J., Värri, A. J., Grönman, A. and Lohtander, M.** (2018). Fabrication of surface with reduced friction using nanosecond laser. *Procedia Manufacturing*, Vol. 17, pp. 14-21.
- Kordy H.** (2015). Process abilities of the riblet-coating process with dual-cure lacquers. *CIRP Journal of Manufacturing Science and Technology*, Vol. 11, pp. 1-9.
- Kostina, G. N., Sokolov, V. E., Romanenko, E. V., Sidorova, T. N., Tarchevskaya, V. A. and Chernova, O. F.** (1996). Hydrophobicity of penguin feather structures (Aves Sphenisciformes). *Zoologichskii Zhurnal*, Vol. 75, No. 2, pp. 237-248.
- Kulp, F. B., D'Alba, L., Shawkey, M. D. and Clarke, J. A.** (2018). Keratin nanofiber distribution and feather microstructure in penguins. *The Auk*, Vol. 135, pp. 777–787.
- Lang, A. W., Bradshaw, M. T., Smith, J. A., Wheelus, J. N., Motta, P. J., Habegger, M. L. and Hueter, R. E.** (2014). Movable shark scales act as a passive dynamic microroughness to control flow separation. *Bioinspiration & Biomimetics*, Vol. 9, 036017.
- Lovvorn, J. R., Liggins, G. A., Borstad, M. H., Calisal, S. M. and Mikkelsen, J.** (2001). Hydrodynamic drag of diving birds: Effects of body size, body shape and feathers at steady speeds. *The Journal of Experimental Biology*, Vol. 204, pp. 1547-1557.
- Lufthansa Technik.** (2021). Nature as a role model: Lufthansa Group and BASF roll out sharkskin technology. https://www.lufthansa-technik.com/de/press-releases/-/asset_publisher/Xix57wMv0mow/content/pm_sharkskin_aeroshark_lhcargo (Retrieved on April 15, 2022).
- Luna-Jorquera, G. and Culik, B. M.** (1999) Diving behavior of Humboldt penguins *Spheniscus humboldti* in northern Chile. *Marine Ornithology*, Vol. 27, pp. 67-76.
- Maeda, K.** (2011). Development of automotive aerodynamics and approach trend. *Wind Engineers, JAWE*, Vol. 36, No. 3.
- Mattern, T., Pütz, K., Garcia-Borboroglu, P., Ellenberg, U., Houston, D. M., Long, R., Lüthi, B. and Seddon, P. J.** (2018). Marathon penguins—Reasons and consequences of long-range dispersal in Fiordland penguins/Tawaki during the premolt period. *PLoS One*, Vol. 13, e0198688.
- Min, T. and Kim, J.** (2004). Effects of hydrophobic surface on skin-friction drag. *Physics of Fluids*, Vol. 16, No. 7, pp. L55-L58.

540 **NASA Langley Research Center.** (1993). NASA riblets for starts & stripes.
541 <https://www.nasa.gov/centers/langley/news/factsheets/Riblets.html> (Retrieved on April 15, 2022).

542 **Sasamori, M., Mamori, H., Iwamoto, K. and Murata, A.** (2014). Experimental study on drag-
543 reduction effect due to sinusoidal riblets in turbulent channel flow. *Experiments in Fluids*, Vol. 55, No.
544 1828.

545 **Sato, K., Shiomi, K., Marshall, G., Kooyman, G. L. and Ponganis, P. J.** (2011). Stroke rates and
546 diving air volumes of emperor penguins: implications for dive performance. *The Journal of Experimental*
547 *Biology*, Vol. 214, pp. 2854-2863.

548 **Sato, K., Watanuki, Y., Takahashi, A., Miller, P. J. O., Tanaka, H., Kawabe, R., Ponganis, P. J.,**
549 **Handrich, Y., Akamatsu, T., Watanabe, Y., et al.** (2007). Stroke frequency, but not swimming speed, is
550 related to body size in free-ranging seabirds, pinnipeds and cetaceans. *Proceedings of the Royal Society B:*
551 *Biological Sciences*, Vol. 274, pp. 471–477.

552 **Schlichting, H.** (1979). Boundary-Layer Theory 7th ed., Springer.

553 **Stenzel, V., Wilke, Y. and Hage, W.** (2011). Drag-reducing paints for the reduction of fuel
554 consumption in aviation and shipping. *Progress in Organic Coatings*, Vol. 70, pp. 224-229.

555 **Sundin, J. and Bagheri, S.** (2019). Interaction between hairy surfaces and turbulence for different
556 surface time scales. *Journal of Fluid Mechanics*, Vol. 861, pp.556-584.

557 **Szodruch, J.** (1991). Viscous drag reduction on transport aircraft. *AIAA 29th Aerospace Science*
558 *Meeting*.

559 **Tiainen, J., Grönman, A., Jaatinen-Värri, A. and Pyy, L.** (2020). Effect of nonideally
560 manufactured riblets on airfoil and wind turbine performance. *Renewable Energy*, Vol. 155, pp. 79-89.

561 **Walsh, M. J. and Lindemann, A. M.** (1984). Optimization and application of riblets for turbulent
562 drag reduction. *AIAA 22nd Aerospace Sciences Meeting*, pp. 347-356.

563 **Watanabe, Y. Y., Sato, K., Watanuki, Y., Takahashi, A., Mitani, Y., Amano, M., Aoki, K.,**
564 **Narazaki, T., Iwata, T., Minamikawa, S. and Miyazaki, N.** (2011). Scaling of swim speed in breath-hold
565 divers. *Journal of Animal Ecology*, Vol. 80, pp. 57-68.

566 **Watanuki, Y., Wanless, S., Harris, M., Lovvorn, J. R., Miyazaki, M., Tanaka, H. and Sato, K.**
567 (2006). Swim speeds and stroke patterns in wing-propelled divers: a comparison among alcids and a
568 penguin. *Journal of Experimental Biology*, Vol. 209, pp. 1217-1230.

569 **Wienecke, B., Robertson, G., Kirkwood, R. and Lawton, K.** (2007). Extreme dives by free-
570 ranging emperor penguins. *Polar Biology*, Vol.30, pp. 133–142.

571 **Williams, C. L., Hagelin, J. C., and Kooyman, G. L.** (2015). Hidden keys to survival: the type,
572 density, pattern and functional role of emperor penguin body feathers. *Proceedings of the Royal Society B:*
573 *Biological Sciences*, Vol. 282, 20152033.

574 **Zhang, Y. F. and Yin, Y. H.** (2019). Study on riblet drag reduction considering the effect of sweep
575 angle. *Energies*, Vol. 12, 3386.

Figures and tables

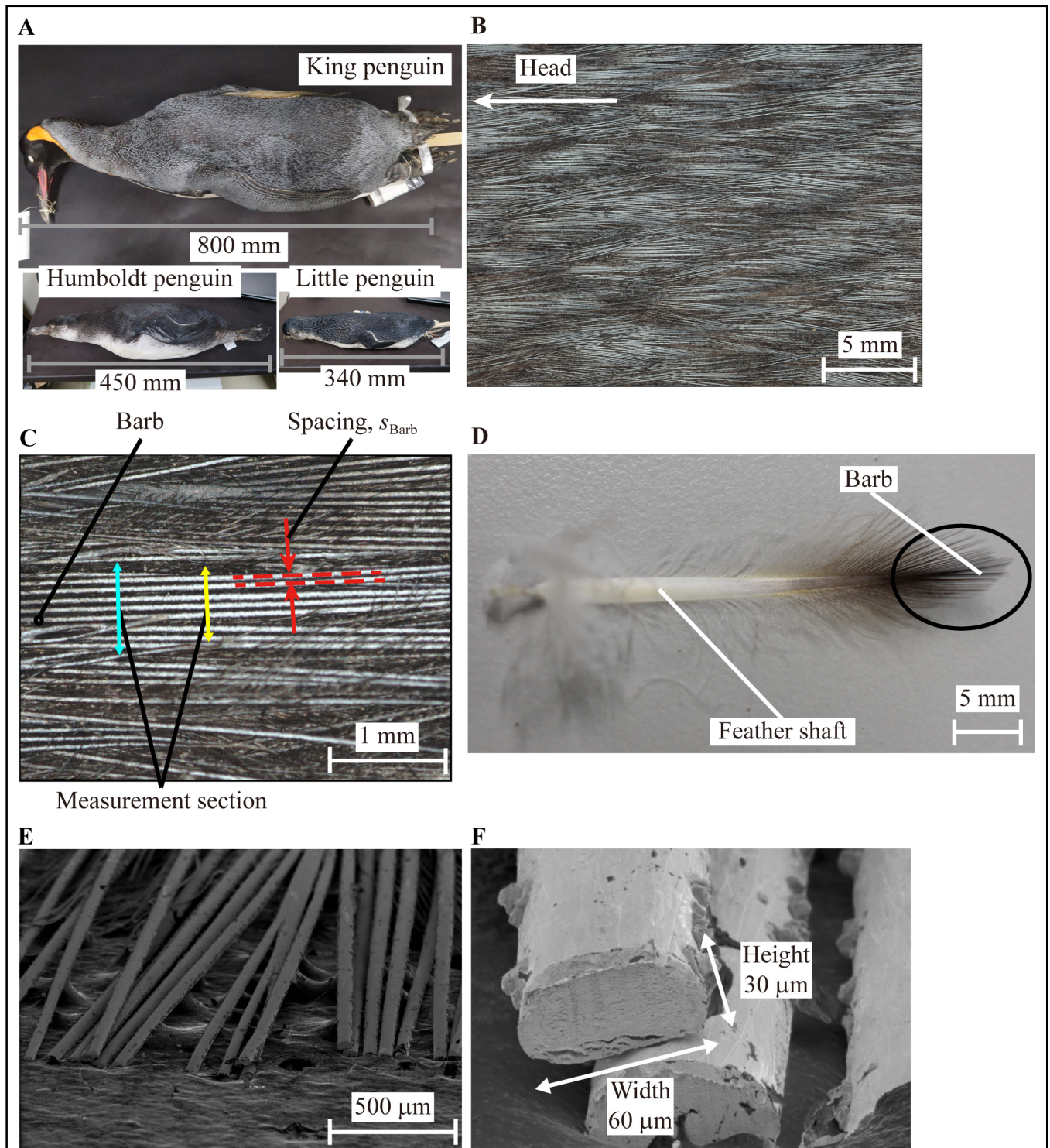


Figure 1. Morphology of penguin body feathers. (A) Longitudinal lengths of the museum specimens of the king, Humboldt, and little penguins. (B, C) Example photos of the dorsal surface from the king penguin specimen taken at 0.5 m from the head. The “measurement section” in the figure indicates the location where the spacing and width of barbs were measured. (D) A single body feather of a gentoo penguin. (E) SEM image of the gentoo penguin’s barbs. The tips of the barbs were cut with a scalpel. (F) The cross-sectional shape of the gentoo penguin barb.

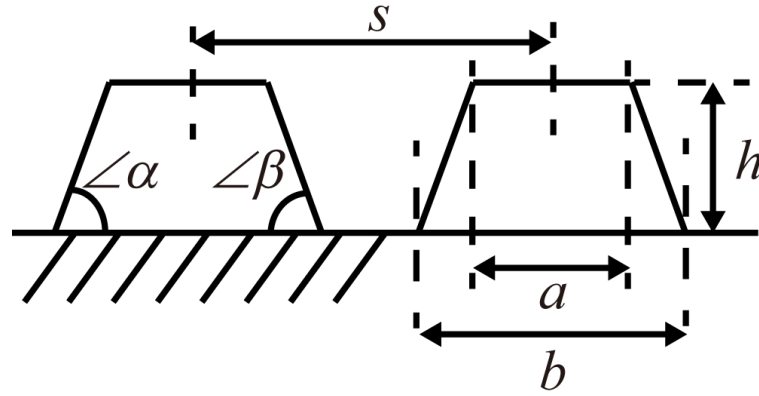


Figure 2. Cross-sectional schematic of the penguin-mimetic riblet.

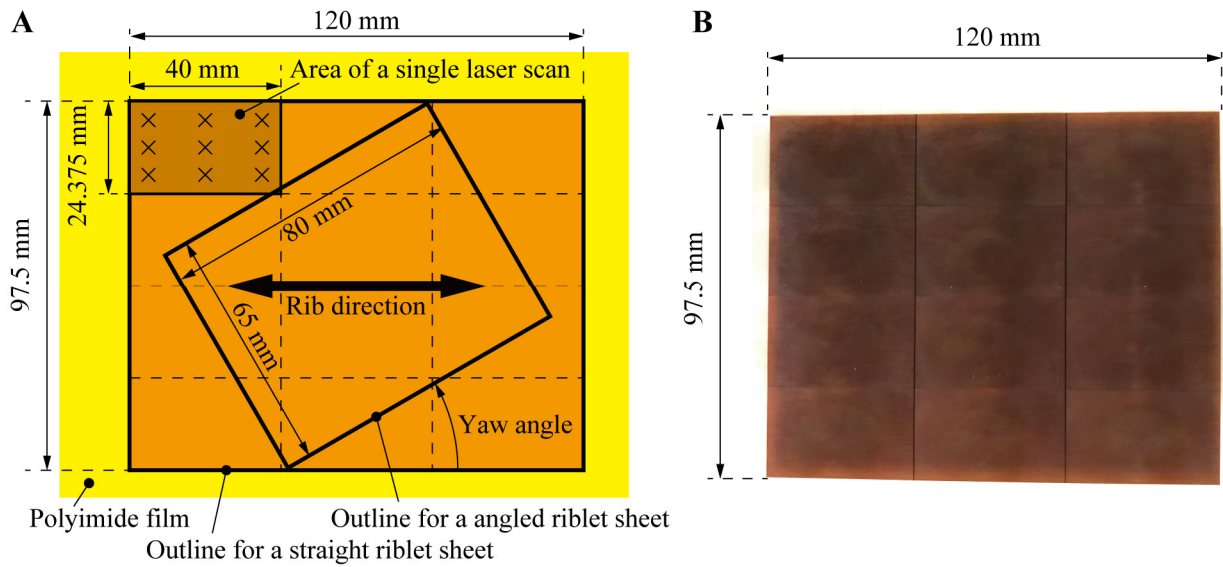


Figure 3. Planar dimensions of riblet sheets. (A) Outline design of the riblet sheet. A laser scanning machine created the riblet area of 40 mm by 24.375 mm. By shifting the worktable of the machine and repeating the scanning, the riblet area of 120 mm by 97.5 mm was formed. To create an angled riblet sheet, an inclined rectangular outline of 80 mm by 65 mm was cut out. × marks indicate the locations for 3D shape measurement of the riblet. (B) Photograph of a fabricated riblet sheet with the straight riblet.

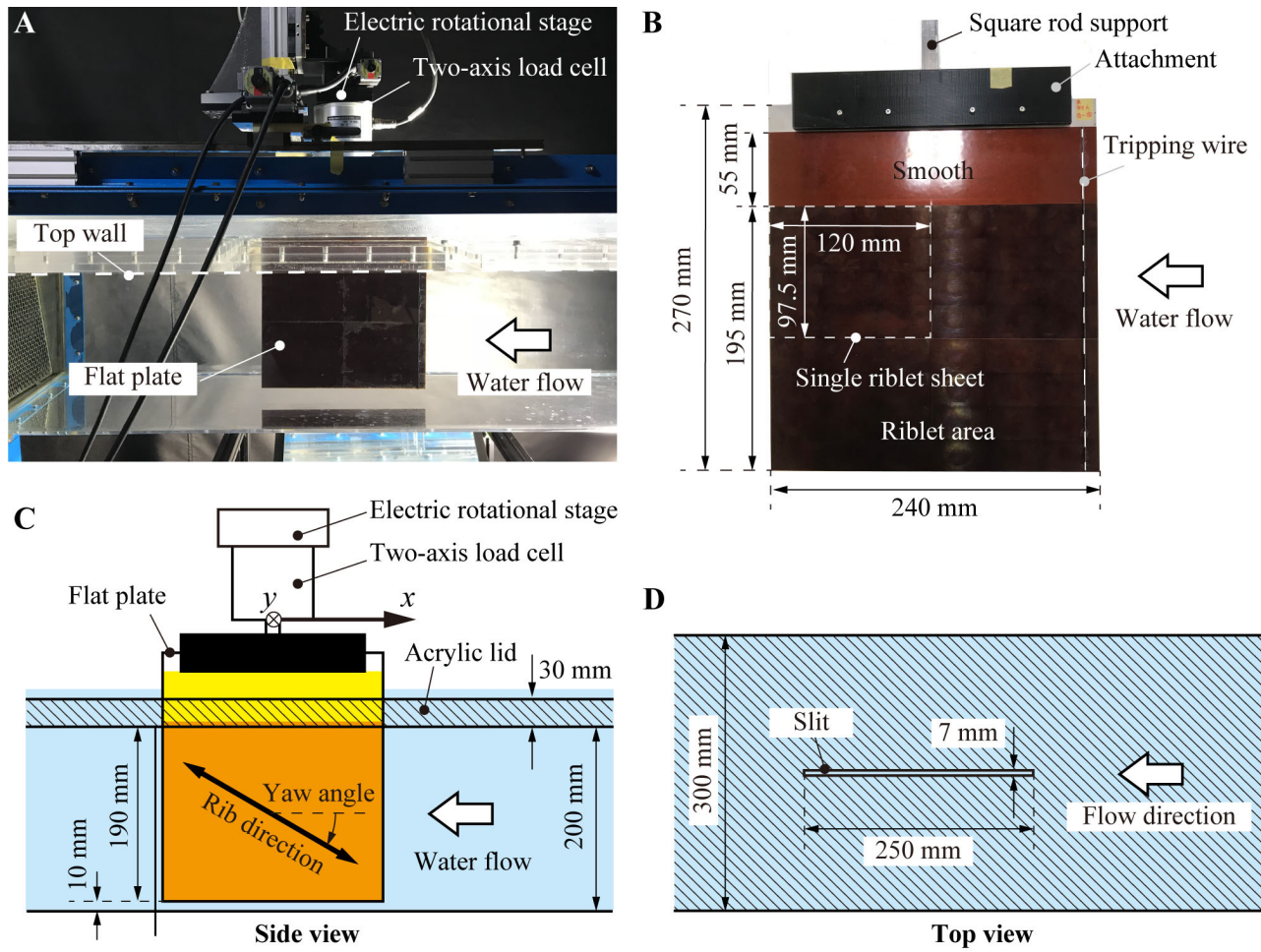


Figure 4. Experimental setup of the drag measurement in a water tunnel. (A, C) Sideview photograph and schematic of the flat plate inserted in the water tunnel. (B) Sideview photograph of the flat plate with the straight riblet. (D) Top view schematic of the slit of the water tunnel for insertion of the plate.

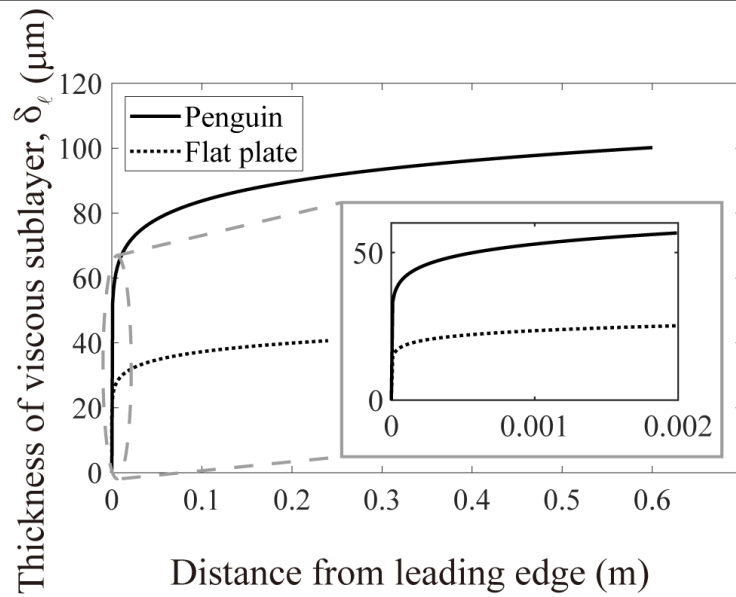


Figure 5. Thickness of the viscous sublayer of the turbulent boundary layer calculated using flat-plate theory. The solid line represents the penguin flow condition, and the dotted line represents the flat plate flow condition in the water tunnel. The graph for the near leading edge is inserted at the bottom right.

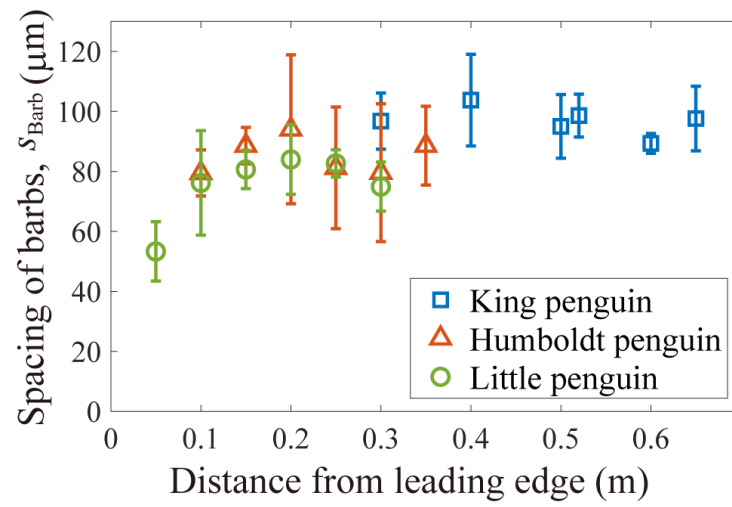


Figure 6. The measured spacing of the barbs for the three penguin specimens. The vertical bar indicates the standard deviation.

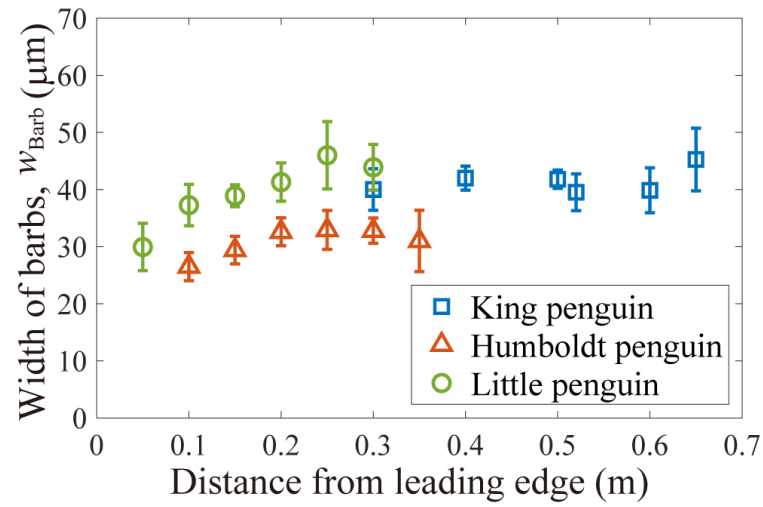


Figure 7. The measured widths of the barbs for the three penguin specimens. The vertical bar indicates the standard deviation.

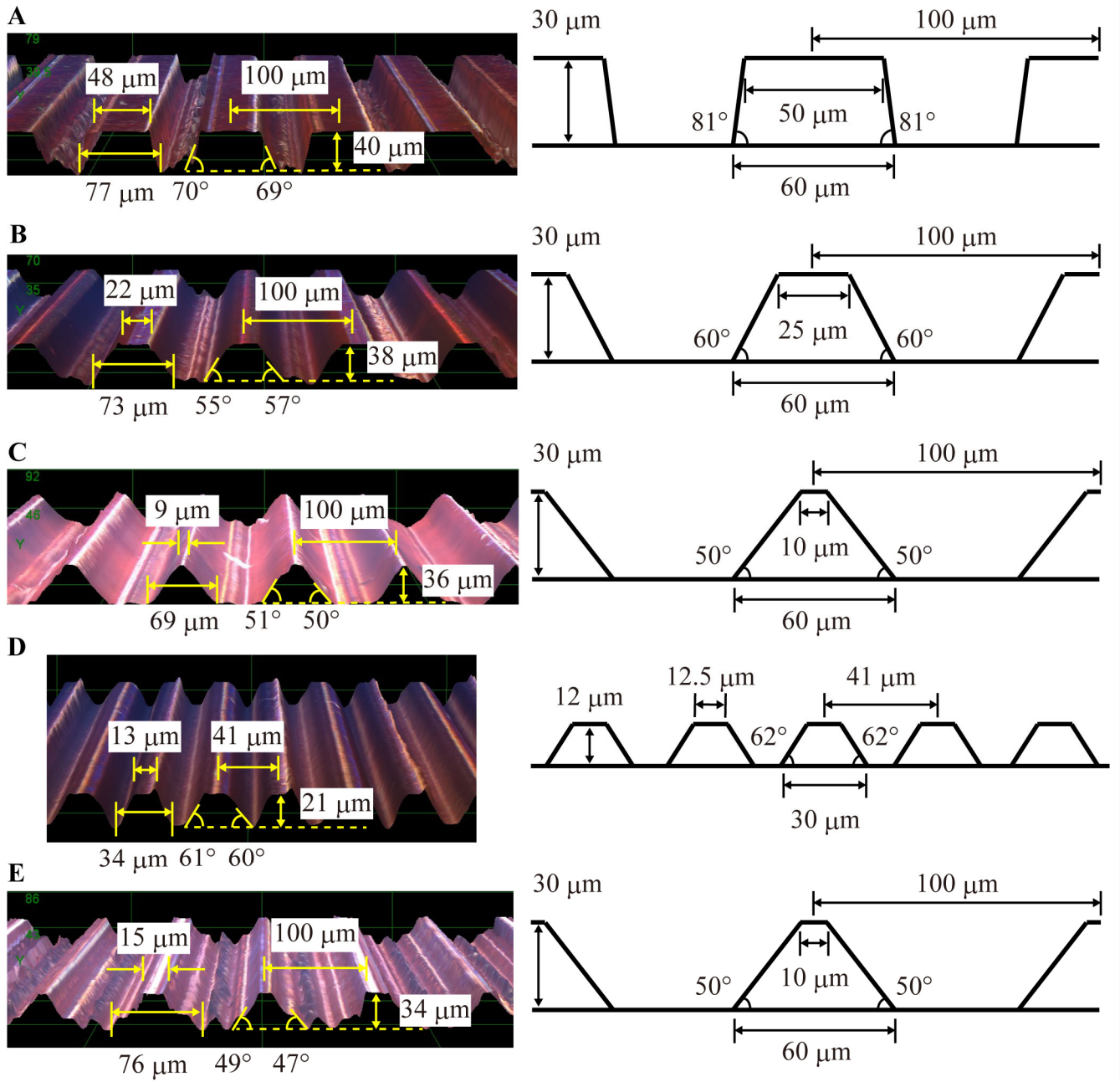


Figure 8. Measured 3-D surface shapes of the actual- and small-scale riblets. (A) Wide-ridge riblets. (B) Medium-ridge riblets. (C) Narrow-ridge riblets. (D) Small-scale riblets. (E) Narrow-ridge riblets in the central location of Fig. 3(A). The design schematic for each riblet is presented on the right.

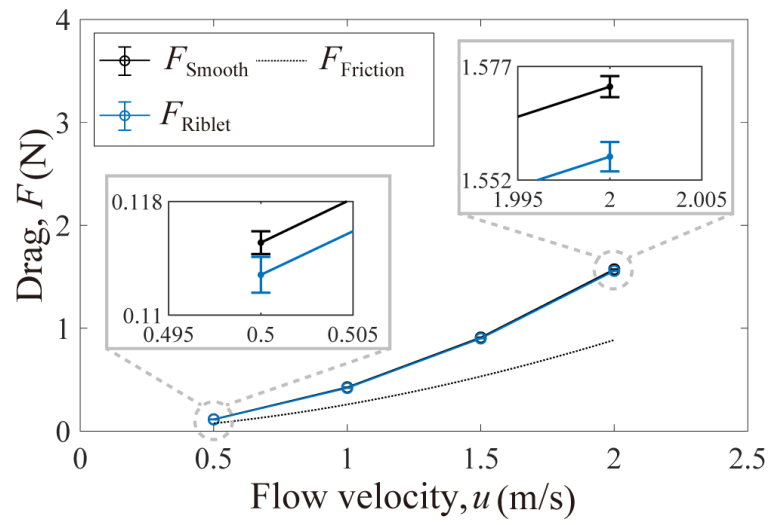


Figure 9. Measured drag of the smooth flat plate (open circles and black line), small-scale riblet (open circles and blue line) and the theoretical calculation of the friction drag of a flat plate (dashed line).

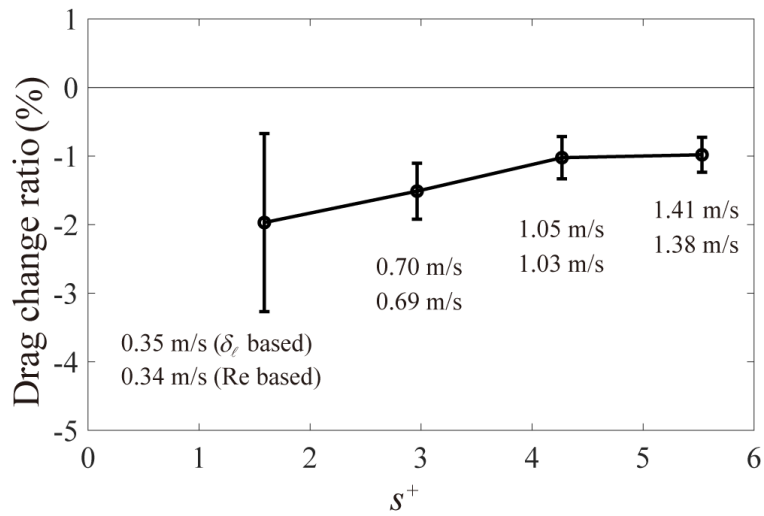


Figure 10. Measured drag-change ratio of the small-scale riblet. The error bars represent the uncertainty U_{RSS} (ANSI/ASME, 1987) (95% coverage). The numbers next to each plot are the corresponding flow speeds based on the Re and $\delta_{\ell, \text{mean}}$.

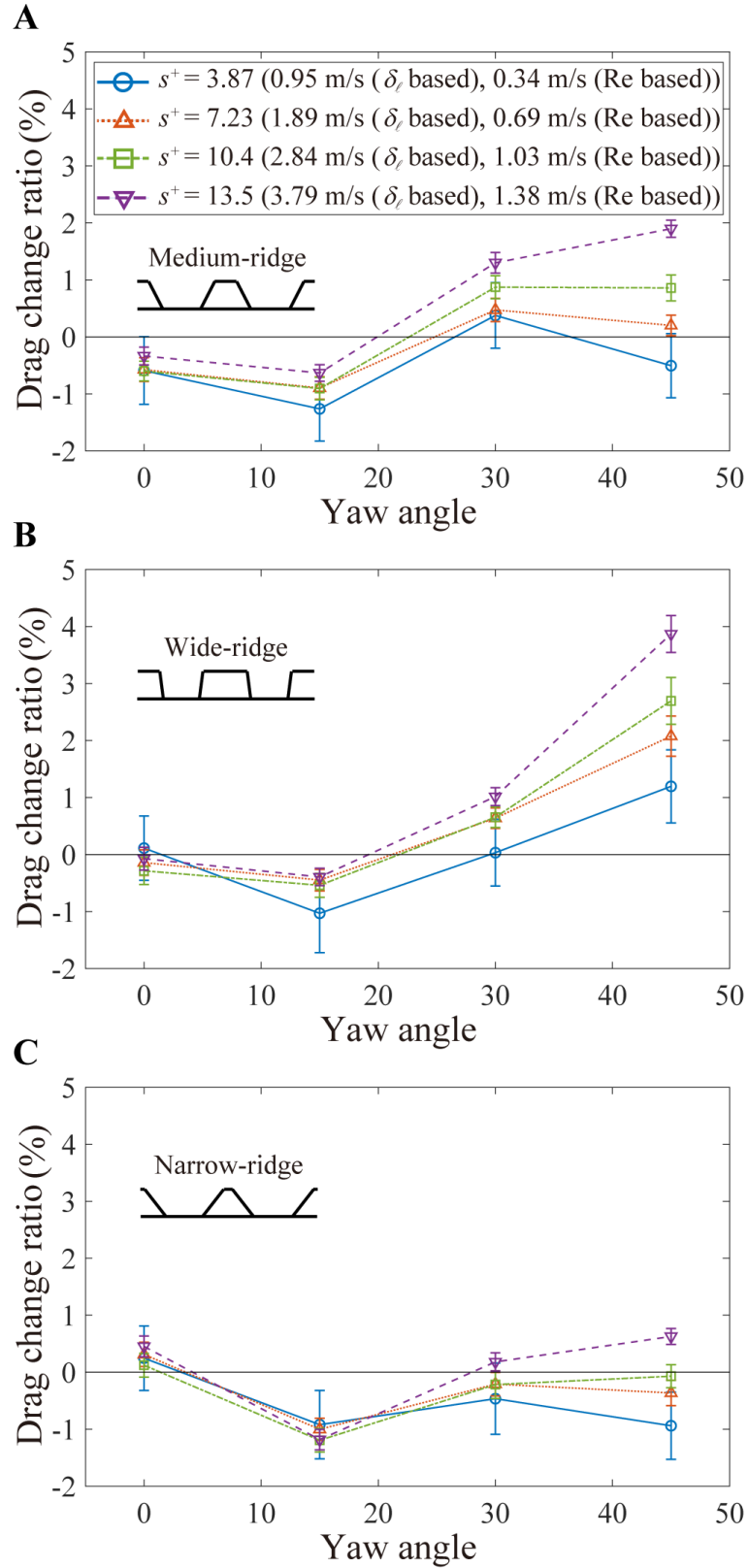


Figure 11. Measured drag-change ratio varying with the yaw angle. (A) Medium-ridge riblets. (B) Wide-ridge riblets. (C) Narrow-ridge riblets. The error bars represent the uncertainty U_{RSS} (ANSI/ASME, 1987) (95% coverage). The corresponding flow speeds based on the Re and $\delta_{l, \text{mean}}$ are displayed in the graph legend.

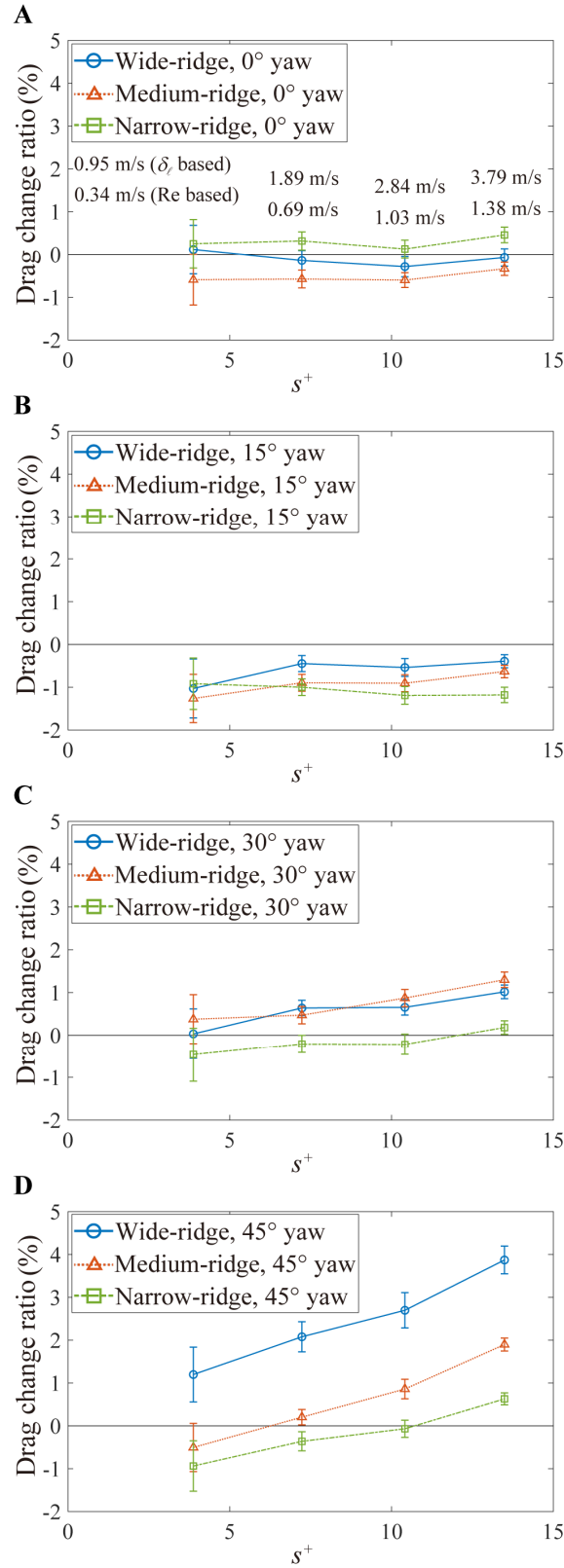


Figure 12. Measured drag-change ratio varying with s^+ . (A) Yaw angle of 0°. (B) Yaw angle of 15°. (C) Yaw angle of 30°. (D) Yaw angle of 45°. The error bars represent the uncertainty U_{RSS} (ANSI/ASME, 1987) (95% coverage). The numbers next to each plot are the corresponding flow speeds based on the Re and $\delta_{\ell, \text{mean}}$.

Table 1. Flow conditions for the gentoo penguin and water tunnel.

	Water temperature (°C)	Length (mm)	Flow speed (m/s)	Kinematic viscosity (m ² /s)	Reynolds number
Penguin	15	600	1.4	1.25×10 ⁻⁶	6.75×10 ⁵
			2.0		6.64×10 ⁵
Flat plate	35	240	1.5	7.23×10 ⁻⁷	4.98×10 ⁵
			1.0		3.32×10 ⁵
			0.5		1.66×10 ⁵

Table 2. Design values and measurement results for the actual- and small-scale riblets.

Parameters		s (μm)	h (μm)	a (μm)	b (μm)	α (°)	β (°)	h/s	a/b	
Design values	Actual-scale	Wide-ridge	100	30	50	60	81	81	0.3	0.83
		Medium-ridge	100	30	25	60	60	60	0.3	0.42
		Narrow-ridge	100	30	10	60	50	50	0.3	0.17
	Small-scale	41	12	12.5	30	62	62	0.29	0.42	
Measurement results*	Actual-scale	Wide-ridge	100±0.2	40±1.3	48±3.0	77±2.1	70±4.6	69±3.6	0.4	0.62
		Medium-ridge	100±0.2	38±3.0	22±4.9	73±1.6	55±2.0	57±1.7	0.38	0.30
		Narrow-ridge	100±0.1	36±1.9	9±3.0	69±3.1	51±4.0	50±2.7	0.36	0.13
	Small-scale	41±0.1	21±2.2	13±4.3	34±3.0	61±6.4	60±7.9	0.51	0.38	

*The average values and standard deviations are presented. The number of measurement locations for each sheet was 9.